

Wien2wannier: From linearized augmented plane waves to maximally localized Wannier functions

Jan Kuneš^{a,b}, Ryotaro Arita^{c,d}, Philipp Wissgott^e, Alessandro Toschi^e, Hiroaki Ikeda^f
Karsten Held^e

^a*Theoretical Physics III, Center for Electronic Correlations and Magnetism, Institute of Physics, University of Augsburg, Augsburg 86135, Germany*

^b*Institute of Physics, Academy of Sciences of the Czech Republic, Cukrovarnická 10, CZ-162 53 Prague 6, Czech Republic*

^c*CREST, JST, and Department of Applied Physics, University of Tokyo, Hongo, Tokyo 113-8656, Japan*

^d*Department of Applied Physics, University of Tokyo, Hongo, Tokyo 113-8656, Japan*

^e*Institute for Solid State Physics, Vienna University of Technology, Vienna, Austria*

^f*Department of Physics, Kyoto University, Kyoto, 606-8502, Japan*

Abstract

We present an implementation of interface between the full-potential linearized augmented plane wave package Wien2k and the wannier90 code for the construction of maximally localized Wannier functions. The FORTRAN code and a documentation is made available and results are discussed for SrVO₃, Sr₂IrO₄ (including spin-orbit coupling), LaFeAsO, and FeSb₂.

Key words: electronic structure, density functional theory, Wannier functions, augmented plane waves, Wien2K, wannier90

1. Introduction

In recent years, we have seen a revival of Wannier’s idea [1] to express the single electron excitations in a periodic potential in terms of “orthogonal ‘atomic’ wave functions”, later coined Wannier functions. While the calculation of bandstructures as, e.g., within density functional theory (DFT) [2] is most efficiently performed in the basis of extended wave functions indexed by reciprocal-space vectors \mathbf{k} , the complementary Wannier picture is often useful - if not essential. The latter does not only provide insight into the nature of chemical bonding, but the localized Wannier orbitals are more suitable to describe physical phenomena where the local aspect is important. These range from the dielectric polarization [3], e.g., in the context of ferroelectrics [4,5], and orbital polarization [6] to molecular dynamics [7] and transport through nano structures [8,9].

Also to describe electronic correlations beyond the local density approximation (LDA) to DFT, Wannier-like orbitals are very helpful. Here they allow us to limit the interactions to a computationally manageable subspace, such as the local interactions between electrons on the same transition-metal atom in the d -orbitals. The on-site term represents not only the largest contribution to the interaction, but typically gives

* Corresponding author.

Email address: kunes@fzu.cz (Jan Kuneš).

raise to the dominant electronic correlations. This is because inter-site interaction terms yield mainly the Hartree contribution if the number of neighbors is large [10], and this is already included in LDA. The concept of Wannier functions has hence found its use also in materials specific many-body calculation with the LDA+dynamical mean field theory (DMFT) approach [11]. The first LDA+DMFT calculations made use of downfolded linearized muffin tin orbitals (LMTO) [12] and N th order muffin tin orbitals (NMTO) [13] which exploit the local character of the basis functions. For other bandstructure methods with bases of extended orbitals a transformation to Wannier functions is needed.

While the conversion from Bloch to Wannier functions is essentially a Fourier transformation, there remains an arbitrariness in choice of the phases of the Bloch functions; i.e., this conversion is not unique. This arbitrariness can be used to construct localized orbitals. Marzari and Vanderbilt [14,15] developed a procedure to fix the phases (and further \mathbf{k} -dependent unitary transformations) so that the resulting Wannier orbitals minimal spread around their centers. Together with coworkers, they developed a corresponding program package `wannier90` [16].

Since then the maximally localized Wannier functions (MLWF) have been implemented for many DFT/LDA program packages ranging from plane waves to LMTO [17,18] and linearized augmented plane waves (LAPW) in the FLAPW [19] and FLEUR code [20]. Alternatives to MLWF have been proposed as well, including the recent Wannier function projection [21,22] where the overlap of the Bloch functions with the d - or f -orbitals within the atomic or muffin tin spheres defines the Wannier functions. This approach has been implemented for LMTO [22] and by Aichhorn *et al.* [23] for the FLAPW of the Wien2K code [24]. While this approach is somewhat easier to implement, the final Wannier functions are no longer uniquely defined and may differ considerably. With a clever choice of the functions to project onto, results very similar to MLWF can be obtained.

In this paper, we present an interface [25] between Wien2K [24] implementation of the FLAPW method and the `wannier90` code [16]. This interface generates the `wannier90` input files (`.eig`, `.mmn`, `.amn`) from the Wien2K electronic structure. Furthermore, we provide a code for the generation of MLWFs in direct space, primarily useful for visualization. The interface consists of FORTRAN90 programs (tested for `gfortran` and `ifort`; hitherto not parallelized) with additional shell and python scripts to simplify the work-flow. A manual is available at [25]; the work-flow will be briefly described in Section 2.4. The runtime of the main program (`w2w`) was 4.6 s for a simple test system such as SrVO_3 with 64 \mathbf{k} -points, running under Linux with a 64-bit Intel Xeon 3 GHz 4GB RAM. For visualization, an output to XCrystDen [26] is also provided.

The following sections are organized as following: In Section 2, we discuss the theoretical background and equations, in particular the projection onto maximally localized Wannier function (MLWF) in Section 2.1 and the LAPW of Wien2K in Section 2.2. Some practical considerations are presented in Section 2.3. The workflow of our Wien2Wannier interface is outlined in Section 2.4. In Section 3, we present exemplarily some applications of the code. We start with the simple bandstructure of SrVO_3 in Section 3.1 to demonstrate how the choice of the energy window affects the shape of WFs and the corresponding tight-binding Hamiltonian. Sr_2IrO_4 with an idealized structure illustrates in Section 3.2 the construction of WFs in a system with strong spin-orbit coupling leading to orbitals with complex phases. In Section 3.3, LaFeAsO is used to show the utility of WFs for backfolding of the electronic bandstructures, in order to obtain the simplest possible \mathbf{k} -space representation of the electronic structures. Finally, in Section 3.4, we show the application of the code to a material with low site-symmetry by the example of FeSb_2 .

2. Theory

2.1. Wannier functions

Following Refs. [14,15] we define the Wannier orbitals $w_{n\mathbf{R}}(\mathbf{r})$ in the R 'th unit cell through a unitary transformation $U^{(\mathbf{k})}$ of the Bloch eigenstates $\psi_{n\mathbf{k}}(\mathbf{r})$ of the periodic Hamiltonian:

$$w_{n\mathbf{R}}(\mathbf{r}) = \frac{V}{(2\pi)^3} \int_{BZ} e^{-i\mathbf{k}\cdot\mathbf{R}} \left(\sum_n U_{nm}^{(\mathbf{k})} \psi_{n\mathbf{k}}(\mathbf{r}) \right). \quad (1)$$

In the following the overall phases of the Bloch functions are assumed to be arbitrary, except of the periodic gauge constraint $\psi_{m\mathbf{k}+\mathbf{G}} = \psi_{m\mathbf{k}}$ for \mathbf{G} being a reciprocal lattice vector. According to the Bloch theorem the function $\psi_{n\mathbf{k}}$ factorizes into a product of the plane wave $\exp(i\mathbf{k} \cdot \mathbf{r})$ and a periodic function $u_{n\mathbf{k}}$:

$$\psi_{n\mathbf{k}} = e^{i\mathbf{k} \cdot \mathbf{r}} u_{n\mathbf{k}}. \quad (2)$$

We are looking for that $U^{(\mathbf{k})}$ which yields MLWFs, i.e., minimizes the spread (variance)

$$\sum_m \langle w_{m\mathbf{R}}(\mathbf{r}) | \mathbf{r}^2 | w_{m\mathbf{R}}(\mathbf{r}) \rangle - \langle w_{m\mathbf{R}}(\mathbf{r}) | \mathbf{r} | w_{m\mathbf{R}}(\mathbf{r}) \rangle^2. \quad (3)$$

As the Wannier orbitals are expressed in terms of the Bloch wave functions in Eq. (1), we need to calculate the following overlap integrals on a uniform \mathbf{k} -mesh in the Brillouin zone (BZ):

$$M_{mn}^{(\mathbf{k}, \mathbf{b})} = \langle u_{m\mathbf{k}} | u_{n\mathbf{k}+\mathbf{b}} \rangle \quad (4)$$

$$= \langle \psi_{m\mathbf{k}} | e^{-i\mathbf{b} \cdot \mathbf{r}} | \psi_{n\mathbf{k}+\mathbf{b}} \rangle \quad (5)$$

For further details on how to determine the MLWF from these overlap integrals, we refer the reader to [14,15].

Moreover, for the disentanglement procedure described in [15] and a good starting guess, also overlap integrals with a set of fixed trial orbitals g_n

$$A_{mn}^{(\mathbf{k})} = \langle \psi_{m\mathbf{k}} | g_n \rangle \quad (6)$$

have to be calculated. The evaluation of $M_{mn}^{(\mathbf{k}, \mathbf{b})}$ and $A_{mn}^{(\mathbf{k})}$ in the LAPW basis is the subject of the rest of this section.

2.2. Linearized augmented plane-waves

In the LAPW method, the direct space is divided into two regions: the interstitial space I and the non-overlapping muffin-tin (MT) spheres S_β around the nuclei at \mathbf{R}_β . The Bloch functions are expanded into plane waves in I and into partial atomic waves in the MT spheres

$$\psi_{\mathbf{k}}^\sigma(\mathbf{r}) = \begin{cases} \frac{1}{\sqrt{V}} \sum_{\mathbf{G}} C_{\mathbf{k}}^\sigma(\mathbf{G}) e^{i(\mathbf{k}+\mathbf{G})\mathbf{r}} & \mathbf{r} \in \text{I} \\ \sum_{\ell m} \left(a_{\mathbf{k}, \ell m}^{\beta\sigma} u_{1, \ell}^{\beta\sigma}(r_\beta) + b_{\mathbf{k}, \ell m}^{\beta\sigma} \dot{u}_{1, \ell}^{\beta\sigma}(r_\beta) + c_{\mathbf{k}, \ell m}^{\beta\sigma} u_{2, \ell}^{\beta\sigma}(r_\beta) \right) Y_{\ell m}(\hat{\mathbf{r}}_\beta) & \mathbf{r} \in S_\beta, \end{cases} \quad (7)$$

where $Y_{\ell m}$ are the spherical harmonics and u_1 , \dot{u}_1 , and u_2 are numerically determined functions of the radial variable $r_\beta = |\mathbf{r} - \mathbf{R}_\beta|$, which are defined separately for each MT sphere β , orbital quantum number ℓ and, in spin-polarized calculations, spin projection σ . For simplicity we do not show the dependence of the expansion coefficients $C_{\mathbf{k}}^\sigma$, $a_{\mathbf{k}, \ell m}^{\beta\sigma}$, $b_{\mathbf{k}, \ell m}^{\beta\sigma}$, and $c_{\mathbf{k}, \ell m}^{\beta\sigma}$ on the band index. Both LAPWs and augmented plane waves plus local orbitals (APW+lo) basis sets can be used for our interface. While further details can be found in Ref. [27] we point out two features of the expansion: (i) it is not possible to obtain the periodic part $u_{n\mathbf{k}}$ inside the spheres in a simple straight-forward way from the above expansion of the Bloch function and therefore we used Eq. (5) in actual calculations; (ii) the Bloch function is uniquely defined by $C_{\mathbf{k}}^\sigma(\mathbf{G})$ since the other expansion coefficients are in fact functions of $C_{\mathbf{k}}^\sigma(\mathbf{G})$, defined by the continuity conditions at the surfaces of the MT spheres.

The calculation of $M_{mn}^{(\mathbf{k}, \mathbf{b})}$ naturally splits into the interstitial part and the MT part. To evaluate (5) inside the MT sphere β , the plane-wave $\exp(-i\mathbf{b} \cdot \mathbf{r})$ is expanded into products of spherical harmonics and Bessel functions using the well known formula

$$e^{-i\mathbf{b} \cdot \mathbf{r}} = 4\pi e^{-i\mathbf{b} \cdot \mathbf{R}_\beta} \sum_{\ell} i^\ell j_\ell(br_\beta) \sum_m \bar{Y}_{\ell m}(-\hat{\mathbf{b}}) Y_{\ell m}(\hat{\mathbf{r}}_\beta). \quad (8)$$

Substituting Eqs. (7) and (8) into Eq. (5), one obtains an expression for the contribution of $M_{mn}^{(\mathbf{k}, \mathbf{b})}$ within the MT spheres in terms of products of radial integrals $\int_0^{R_\beta} dr r^2 u_{p, \ell_1}^{\beta\sigma}(r) j_{\ell_2}(br) u_{q, \ell_3}^{\beta\sigma}(r)$; angular integrals

$\langle\langle \bar{Y}_{\ell_1 m_1} Y_{\ell_2 m_2} Y_{\ell_3 m_3} \rangle\rangle$, known as Gaunt numbers; and an additional weight factor given by the corresponding products of the expansion coefficients.

The interstitial contribution $M_{mn}^{(\mathbf{k}, \mathbf{b})}$ on the other hand reads

$$\left\langle \frac{1}{V} \sum_{\mathbf{G}, \mathbf{G}'} \bar{C}_{\mathbf{k}}^m(\mathbf{G}') C_{\mathbf{k}+\mathbf{b}}^n(\mathbf{G}) \langle e^{i(\mathbf{G}-\mathbf{G}') \cdot \mathbf{r}} \rangle_I \right\rangle, \quad (9)$$

where the $\langle \rangle_I$ integration runs over the unit cell with the MT spheres removed, which gives

$$\langle e^{i(\mathbf{G}-\mathbf{G}') \cdot \mathbf{r}} \rangle_I = V \delta_{\mathbf{G}, \mathbf{G}'} - 3V_\beta \sum_{\beta} e^{-i(\mathbf{G}-\mathbf{G}') \cdot \mathbf{R}_\beta} \frac{\sin(x) - x \cos(x)}{x^3} \quad (10)$$

$$\text{where } x = \rho_\beta |\mathbf{G} - \mathbf{G}'|, \quad V_\beta = \frac{4}{3} \pi \rho_\beta^3,$$

and ρ_β is the radius of the MT sphere at \mathbf{R}_β .

The periodic gauge has to be enforced when the integration in Eq. (1) wraps around the Brillouin zone boundary, namely a reciprocal vector \mathbf{G} must be chosen such that $\mathbf{k} + \mathbf{b} - \mathbf{G}$ lies within the Brillouin zone.

The construction of $A_{mn}^{(\mathbf{k})}$ is rather simple if we allow trial orbitals to be non-zero only inside the MT sphere, i.e. of the form

$$g_n = \sum_{\beta} \sum_{\ell m} g_{\ell m}^{\beta}(n) u_{1,\ell}^{\beta}(r_\beta) Y_{\ell m}(\hat{\mathbf{r}}_\beta), \quad (11)$$

where the list of non-zero coefficients $g_{\ell m}^{\beta}(n)$ is provided as input. Using (7) we obtain

$$A_{n'n}^{(\mathbf{k})} = \sum_{\beta} \sum_{\ell m} \left(\bar{a}_{\mathbf{k}, \ell m}^{n'} \langle u_{1,\ell}^{\beta} | u_{1,\ell}^{\beta} \rangle_r + \bar{b}_{\mathbf{k}, \ell m}^{n'} \langle \dot{u}_{1,\ell}^{\beta} | u_{1,\ell}^{\beta} \rangle_r + \bar{c}_{\mathbf{k}, \ell m}^{n'} \langle u_{2,\ell}^{\beta} | u_{1,\ell}^{\beta} \rangle_r \right) g_{\ell m}^{\beta}(n), \quad (12)$$

where $\langle \rangle_r$ denotes the radial integral with $r^2 dr$.

2.3. Practical considerations

In the following we briefly describe the steps taken in computing WFs. We start by generating a uniform \mathbf{k} -mesh in the Brillouin zone (running KGEN with only the identity matrix in the list of symmetry operations) followed by generating the eigenstates using LAPW1. In case of calculations with spin-orbit coupling LAPWSO should be executed. Spin-orbit calculation must be run as formally spin-polarized even if the polarization is zero. Before running the wien2wannier interface code the initialization run of wannier90 must be executed to generate the case.nnkp file. The inputs to wien2wannier specifies the bands in the initial Hilbert space, the number of the bands in the target Hilbert space and the expansions (11) of the target orbitals. The wien2wannier generates the necessary files case.eig, case.mmn and case.amn, which serve as an input for the MLWF construction by wannier90. In case of spin-orbit coupled calculations, a separate run of wien2wannier is executed for each of the two components of the spinor wave function. The corresponding elements of the resulting case.mmn(amn) files are added up to form the total overlap matrices between the spinor functions. The postprocessing of the wannier90 results is, to a large extent, independent of the bandstructure code. However, for plotting the WFs in direct space information on underlying basis functions is necessary. We have modified the LAPW7 code of the Wien2K package to generate direct space WF maps, which uses the transformation between the initial Bloch states and resulting WFs extracted from the wannier90 calculation.

2.4. Computational details

The calculations reported in the following Section were performed with Wien2k [24] code employing the LDA exchange-correlation functional for SrVO₃, Sr₂IrO₄, LaFeAsO and the generalized gradient correction (GGA) for FeSb₂; in all cases the APW+lo basis set [28] was employed. To construct the Wannier orbitals we followed the sequence: (i) self-consistent bandstructure calculation using the irreducible part of the BZ;

(ii) generation of a uniform k-mesh throughout the entire BZ (wien2k) and of the corresponding $\mathbf{k}, \mathbf{k} + \mathbf{b}$ -list (wannier90); (iii) calculation of the Bloch eigenstates and eigenvalues on the new k-mesh (wien2k); (iv) evaluation of the $M_{mn}^{(\mathbf{k}, \mathbf{b})}$ and $A_{mn}^{(\mathbf{k})}$ elements (wien2wannier); (v) generation of MLWFs (wannier90); (vi) post-processing of MLWFs to generate tight-binding bandstructures, hopping integrals, plots of Wannier orbitals (wannier90+wien2k). In case of calculations with spin-orbit coupling the Bloch functions have two non-zero components, indexed with the spin quantum number, with a definite mutual phase. Once the two components are generated, the contributions to $M_{mn}^{(\mathbf{k}, \mathbf{b})}$ and $A_{mn}^{(\mathbf{k})}$ of each component are computed separately along the lines of the previous section and added up at the end. To plot the Wannier orbitals we extract the $U_{mn}^{(\mathbf{k})}$ matrices of Eq. (1) from the wannier90 processing and combine it with the wien2k utility for the generation of the Bloch state on direct space grids.

3. Results

3.1. SrVO_3

SrVO_3 is a thoroughly studied material with a rather simple band structure (see Fig. 1) consisting of isolated groups of bands derived from O- p , V- $d-t_{2g}$ and V- $d-e_g$ orbitals. Therefore it is very well suited as a testing case. We focus on the V- $d-t_{2g}$ states, which (being partially filled) are of most interest. We compare two different settings, i.e., consisting of two choices of the Hilbert space to be represented by the Wannier functions. Namely, the space spanned by (i) t_{2g} bands only and (ii) all the V- d and O- p bands. In both cases, the t_{2g} Wannier functions are orthogonal to the O- p Bloch or Wannier states. In the former case (i) also the hopping integral between the t_{2g} and O states is still zero at the price of more extended Wannier orbitals with a substantial weight at the O sites. Naturally, the larger energy window (ii) clearly allows the construction of more localized WFs as demonstrated in Fig. 2. The Wannier orbitals (i) have visible density on the neighboring O sites, reflecting the mixed character of the t_{2g} bands. In contrast, the orbitals (ii) constructed from the larger energy window do not have any appreciable (visible) density at O sites (on the scale of the figure) since the latter would be now assigned to the O- p orbitals, which are explicitly presented by O-centered Wannier orbitals.

The spatial extent of the Wannier orbitals is also reflected in the hopping integrals, which were calculated by the wannier90 code. With the small energy window (i) the t_{2g} bands are well described when at least nn- and nnn-hoppings is considered (see Fig. 1), which in the $\{xy, yz, zx\}$ basis read

$$t_{100}[\text{meV}] = \begin{pmatrix} -268 & 0 & 0 \\ 0 & -30 & 0 \\ 0 & 0 & -268 \end{pmatrix}, \quad t_{101}[\text{meV}] = \begin{pmatrix} 7 & 10 & 0 \\ 10 & 7 & 0 \\ 0 & 0 & -93 \end{pmatrix}. \quad (13)$$

The remaining directions follow from symmetry considerations. The longest nnn t_{2g} - t_{2g} hopping corresponds to a length of of 5.4 Å. Using the more localized orbitals (ii) we can achieve similar accuracy (see Figure 1) by considering only V-V nn-hopping and V-O nnn-hopping, which translate into a direct spatial cut-off of only 4.3 Å. The obvious price to be paid are larger matrices (14×14 for (ii) vs 3×3 in case (i)). We point out when no spatial cut-offs are introduced, both choices (i) and (ii) represent the t_{2g} bands to the same arbitrarily high accuracy, determined by the size of the k-mesh used to construct the MLWFs.

3.2. Sr_2IrO_4

Sr_2IrO_4 has been recently the subject of intense investigations due to the close connection between the spin-orbit coupling and its Mott-insulating ground state. We use it as a example of a material where spin-orbit coupling substantially modifies the band structure and leads to Wannier orbitals, in which both spin projections are mixed. For sake of simplicity we have performed the calculations using an idealized double-perovskite structure, while the real material is characterized by a tilting of the IrO_6 octahedra. In the

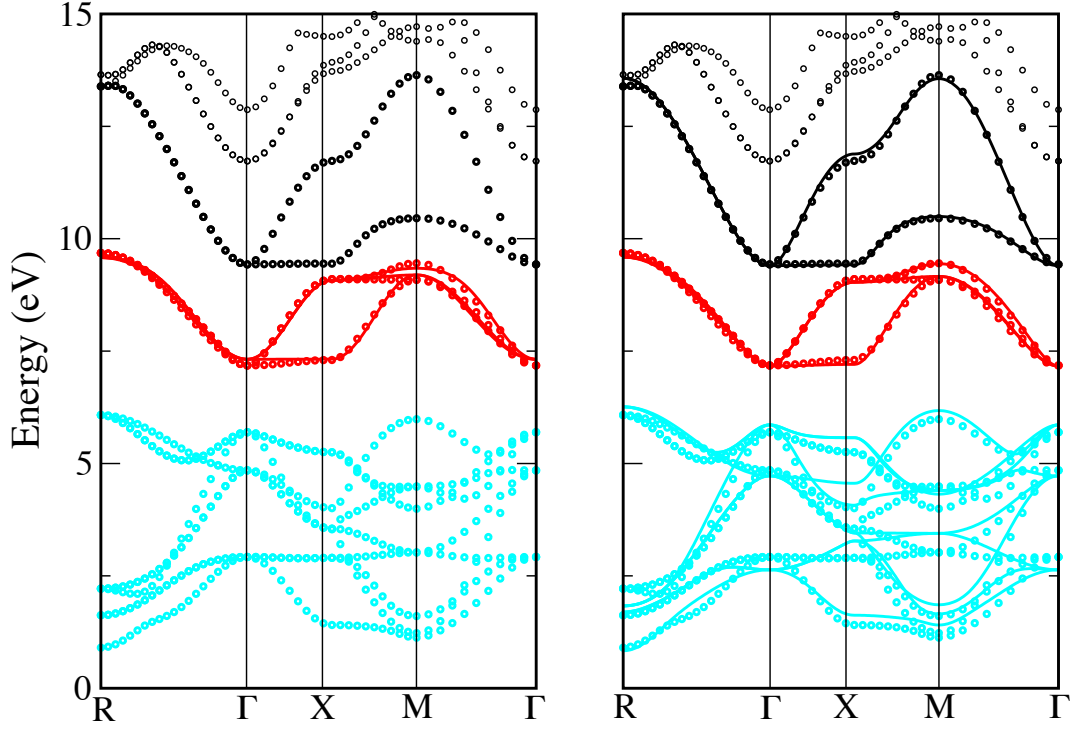


Fig. 1. (color online) LDA band structure of SrVO_3 (circles) with dominant contributions marked with color: O- p (blue), V- $d-t_{2g}$ (red), and V- $d-e_g$ (black). Tight-binding bands obtained from MLWFs for (i)[left panel] only the t_{2g} band (ii)[right panel] all V- d and O- p bands, with spatial cut-offs as described in the text (the Fermi level is at 8.16 eV).

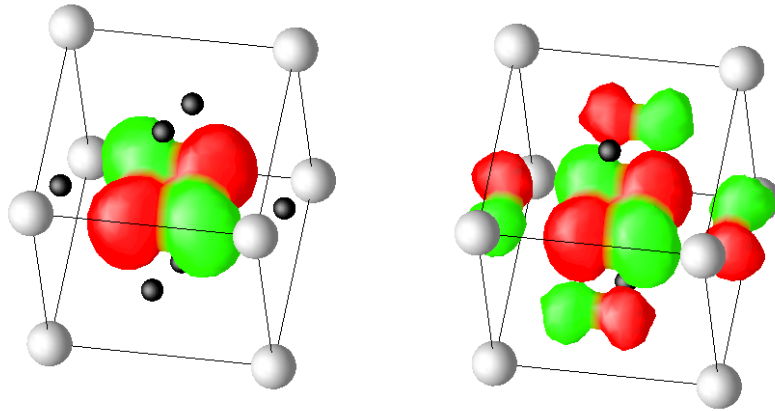


Fig. 2. (color online) LDA band structure of Sr_2IrO_4 (back circles) together with the MLWF tight-binding fit to the $J = 1/2$ bands for different direct space cut-offs; the Fermi level is at 8.2 eV. (left) The xy Wannier orbital plotted as an isosurface of the charge density $|w(\mathbf{r})|^2$ and colored by the sign of $w(\mathbf{r})$. The left panel corresponds to the large energy window (ii) and the right panel to the small energy window (i) for the same isovalue. (right)

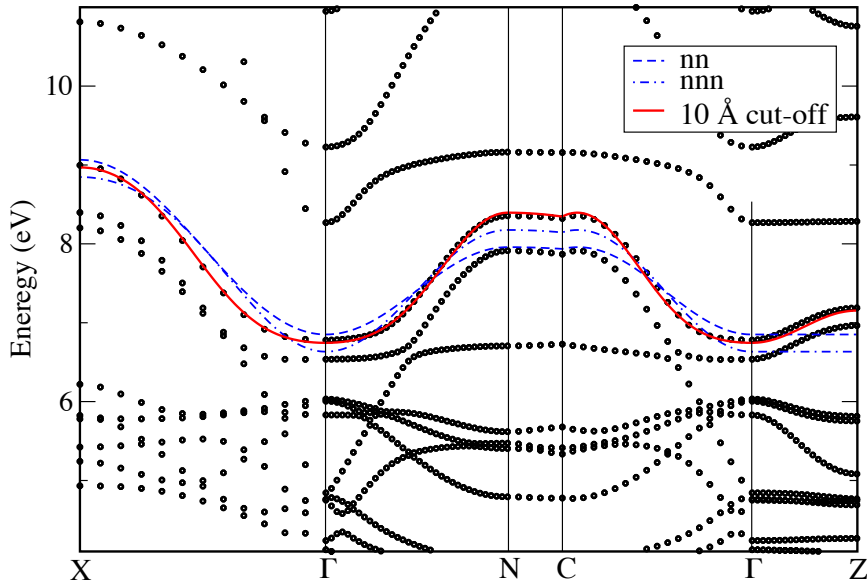


Fig. 3. (color online) LDA band structure of Sr_2IrO_4 (back circles) together with the MLWF tight-binding fit to the $J = 1/2$ bands for different direct space cut-offs (the Fermi level is at 8.2 eV).

following, we discuss the LDA band structure of Sr_2IrO_4 , which represents a crude approximation to correlation effects due to local interactions. Within this picture the electronic structure (see Fig. 4) can be understood by considering the crystal-field splitting, spin-orbit coupling and the inter-site hopping via the manifold of Ir- d bands. The crystal-field splitting, being the largest of the three, opens a gap between the t_{2g} and e_g bands, rendering the latter empty, while the former accommodate one hole per Ir atom. The t_{2g} orbitals may be labeled with a pseudo-spin $I = 1$. The spin-orbit coupling further splits the t_{2g} manifold into a quadruplet and doublet with pseudo-spin $J = 3/2$ and $J = 1/2$, respectively. Since the spin-orbit splitting is rather large the inter-site hopping leads only to moderate mixing of the states with different J . Therefore we may expect the isolated band doublet at the top of the t_{2g} manifold to be predominantly of $J = 1/2$ character. We hence construct the MLWFs for these two bands.

For testing purposes, we have prepared Bloch states on k-grids of sizes $3 \times 3 \times 3$, $5 \times 5 \times 5$, and $7 \times 7 \times 7$. As trial functions we have used the $J_{eff} = 1/2$ orbitals, which adopt the following spinor form with respect to the local coordinate axes pointing towards the O atoms:

$$|\phi_+\rangle \sim \begin{pmatrix} -2Y_{21} \\ Y_{2-2} - Y_{22} \end{pmatrix}, \quad |\phi_-\rangle \sim \begin{pmatrix} Y_{2-2} - Y_{22} \\ 2Y_{2-1} \end{pmatrix}, \quad (14)$$

where we omit the unimportant normalization factor. The results for the three different k-grids were almost identical with minor deviations only for the smallest grid. Due to a clever choice of trial functions, the original spread of the Wannier orbitals as defined in wannier90 actually changed by less than 0.5% during the MLWF optimization. This is consistent with the fact that the resulting MLWFs are essentially $J_{eff} = 1/2$ functions as shown in Fig. 4. In particular, the Wannier orbital, to a very good approximation, consists of a real xy orbital in one spin channel and a complex $(x \pm iy)z$ orbital in the other (\pm) spin channel. Note that the relative phase of the two components is not arbitrary and the corresponding charge density (sum of the spin components) has (approximate) cubic symmetry as expected for a $J_{eff} = 1/2$ orbital.

In Fig. 4 we show convergence of the tight-binding bands to the original band structure with increasing maximum hopping distance. The band dispersion is governed by the nearest- and next-nearest-neighbor hopping and the bands are essentially converged when five coordination spheres are considered, which includes also the out-of-plane hoppings giving rise to the z -axis dispersion. The hopping amplitudes are

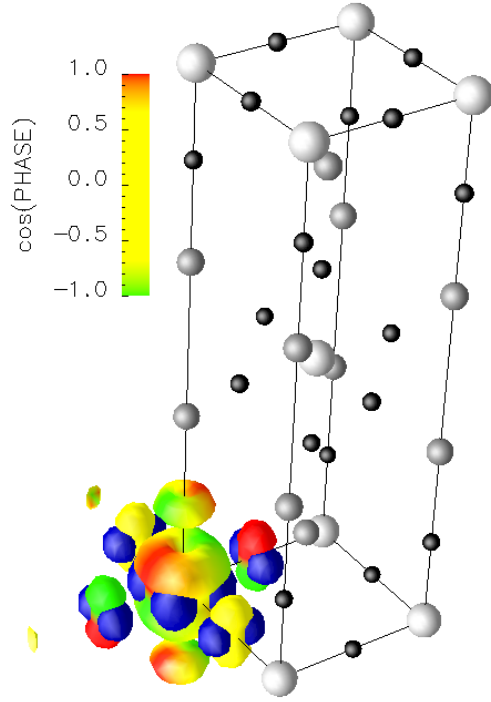


Fig. 4. (color online) Ir $J = 1/2$ Wannier orbital $w_{+, [0,0,0]}(\mathbf{r})$ visualized as a $|w|^2$ isosurface. The almost real \downarrow -spin component is blue, the \uparrow -spin component is colored with cosine of its phase (red=real positive, green=real negative, yellow=imaginary), see color legend bar.

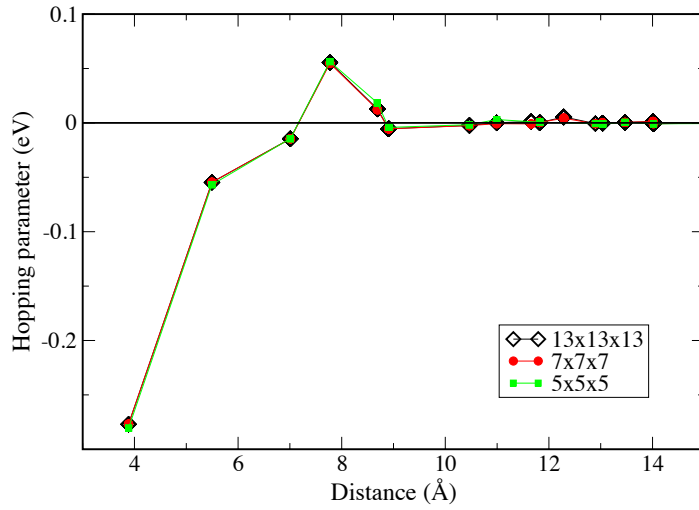


Fig. 5. (color online) The tight-binding hopping integrals of the one-band model as a function of inter-site distance for different BZ grid sizes (the lines are guides for eyes).

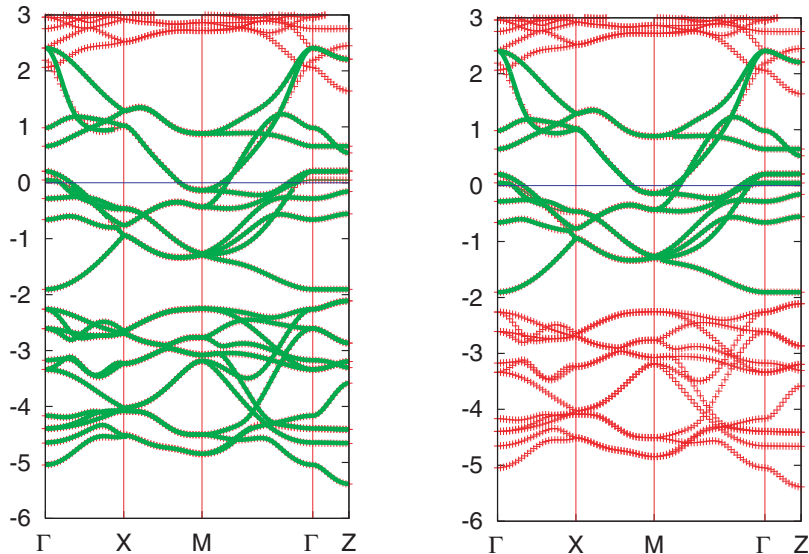


Fig. 6. (color online) LDA band structure of LaFeAsO (red cross symbols) compared with tight-binding bands obtained from MLWFs (green solid lines) for the *dpp* model (left) and the *d* model (right); the Fermi level is set to zero.

summarized in Fig. 5.

3.3. *LaFeAsO*

In 2008, Kamihara *et al.* discovered superconductivity in F-doped LaFeAsO [29], immediately followed by the same finding in related materials. This opened a new field of research inviting many theoretical approaches to be applied, which in turn called for simplified models of the electronic structure capturing the essential chemistry of these systems. These new superconductors commonly have two-dimensional iron pnictide or iron chalcogenite layers, and the low-energy electronic structure around the Fermi level (E_F) consists of heavily entangled bands dominated by the Fe *3d* states (see Fig.6). While the multi-band character renders tight-binding fit impractical, the exact transformation using Wannier functions provides a controlled way of constructing tight-binding models representing the bandstructure to arbitrary accuracy, see Fig.6 and [30–37].

Two types of tight-binding models have been considered for iron pnictides: the *d* model on the basis of Fe *3d*-like orbitals, and *dp* or *dpp* model using the Fe *3d*, pnictogen/chalcogen *p*, and oxygen *p* orbitals. In both cases the corresponding bands are reproduced exactly, as shown in Fig.6, but the behavior of the two models differs if electron-electron interactions are explicitly included. As in the case of SrVO₃, the shape and spread of the Fe *3d* orbitals depends on whether the *d* or *dp* model is used, see Fig.7 and Table 1.

One of the advantages of a tight-binding model, which represents the band dispersion of *ab initio* calculation, is that we can sometimes “unfold” the Brillouin zone. The unit cell of LaFeAsO contains two Fe and As atoms, where one of the As atoms sits above and the other below the Fe plane. Therefore, there are ten Fe *3d* bands. It turns out that the translation symmetry of the tight-binding model is higher and the bandstructure can be unfolded to a five band scheme, corresponding to an effective unit cell with one Fe site. The corresponding bandstructure is shown in Fig.8. The missing translation symmetry between the two Fe sites of the crystallographic unit cell means that the WFs on the two sites are not connected by a simple translation, but by a more general symmetry operation. Obviously, not all operators have the property of the tight-binding Hamiltonian that this does not matter; and therefore the five band model cannot replace the ten band one in general.

| | z^2 | xz | yz | x^2-y^2 | xy | As- pz | As- px | As- py | O- pz | O- px | O- py |
|-----|-------|------|------|-----------|------|----------|----------|----------|---------|---------|---------|
| dpp | 1.82 | 2.13 | 2.13 | 2.41 | 1.74 | | | | | | |
| dpp | 1.08 | 1.34 | 1.34 | 1.30 | 1.01 | 1.93 | 1.98 | 1.98 | 1.27 | 1.30 | 1.30 |

Table 1
Spread of maximally localized Wannier functions for d model and dpp model (in units of \AA).

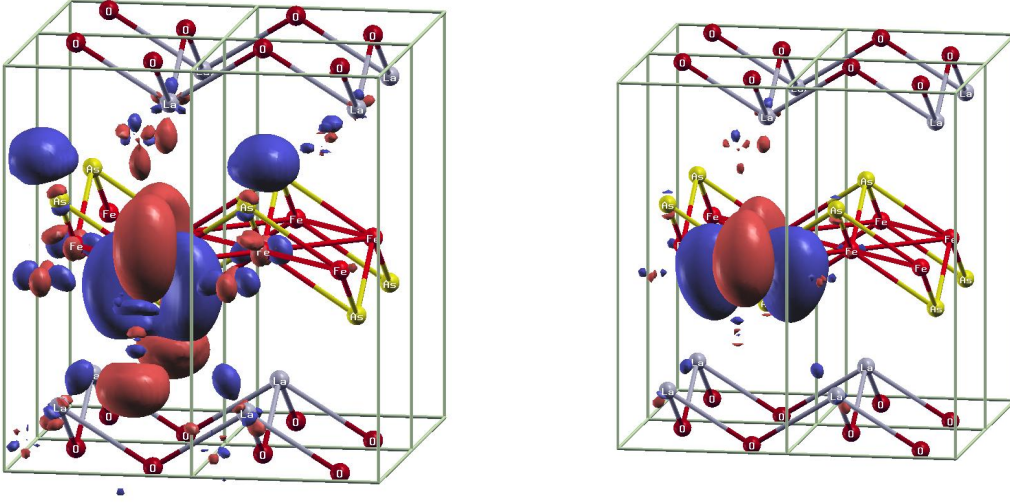


Fig. 7. (color online) Isosurface contours of the x^2-y^2 MLWO for the dpp model (left) and the d -only model (right). The amplitudes of the contour surface are $+0.07 \text{\AA}^{-3/2}$ (red) and $-0.07 \text{\AA}^{-3/2}$ (blue).

In table 2, we list the hopping parameters of the d model. They are very similar to previous studies such as Ref. [30], Ref. [35], of Ref.[37]. It should be noted that since Fe $3d$ bands hybridize with La $5d$, there can be slight difference, depending on whether we use the so-called “inner” window or not, see [37].

| $(\mu, \nu)[\Delta x, \Delta y]$ | [1,0] | [1,1] | [2,0] | [2,1] | [2,2] | σ_y | I | σ_d |
|----------------------------------|-------|-------|-------|-------|-------|------------------|-----|------------|
| (z^2, z^2) | -66 | -8 | -33 | 17 | -15 | + | + | + |
| (z^2, xz) | -72 | 0 | 0 | -2 | 0 | $-(z^2, yz)$ | - | - |
| (z^2, yz) | 72 | -144 | 0 | -3 | -27 | $-(z^2, xz)$ | - | + |
| (z^2, x^2-y^2) | 0 | 160 | 0 | 9 | -15 | - | + | + |
| (z^2, xy) | -297 | 0 | -3 | -20 | 0 | + | + | - |
| (xz, xz) | -198 | 133 | 5 | -6 | 2 | $+(yz, yz)$ | + | + |
| (xz, yz) | 133 | 0 | 24 | -16 | 0 | + | + | - |
| (xz, x^2-y^2) | 167 | 0 | 0 | 14 | 0 | $+(yz, x^2-y^2)$ | - | - |
| (xz, xy) | -252 | 137 | 0 | -9 | 8 | $-(yz, xy)$ | - | + |
| (yz, yz) | -198 | 321 | 5 | -24 | 67 | $+(xz, xz)$ | + | + |
| (yz, x^2-y^2) | 167 | 20 | 0 | 17 | 4 | $+(xz, x^2-y^2)$ | - | + |
| (yz, xy) | 252 | 0 | 0 | 26 | 0 | $-(xz, xy)$ | - | - |
| (x^2-y^2, x^2-y^2) | 154 | 118 | -25 | -30 | -26 | + | + | + |
| (x^2-y^2, xy) | 0 | 0 | 0 | -11 | 0 | - | + | - |
| (xy, xy) | 313 | -68 | -18 | 2 | 1 | + | + | + |

Table 2

Hopping integrals $t(\Delta x, \Delta y; \mu, \nu)$ in units of meV. $[\Delta x, \Delta y]$ denotes the in-plane hopping vector being different for different columns and (μ, ν) the orbitals being different for the rows. The last three columns σ_y , I , and σ_d denote the symmetry transformations necessary to calculate $t(\Delta x, -\Delta y; \mu, \nu)$, $t(-\Delta x, -\Delta y; \mu, \nu)$, and $t(\Delta y, \Delta x; \mu, \nu)$, respectively. Here ‘ \pm ’ means that the corresponding hopping is equal to $\pm t(\Delta x, \Delta y; \mu, \nu)$ in the same row, and ‘ $\pm(\mu', \nu')$ ’ states that the hopping equals $\pm t(\Delta x, \Delta y; \mu', \nu')$ in another (μ', ν') row. Note that there is another symmetry relation $t(\Delta x, \Delta y; \mu, \nu) = t(-\Delta x, -\Delta y; \nu, \mu)$.

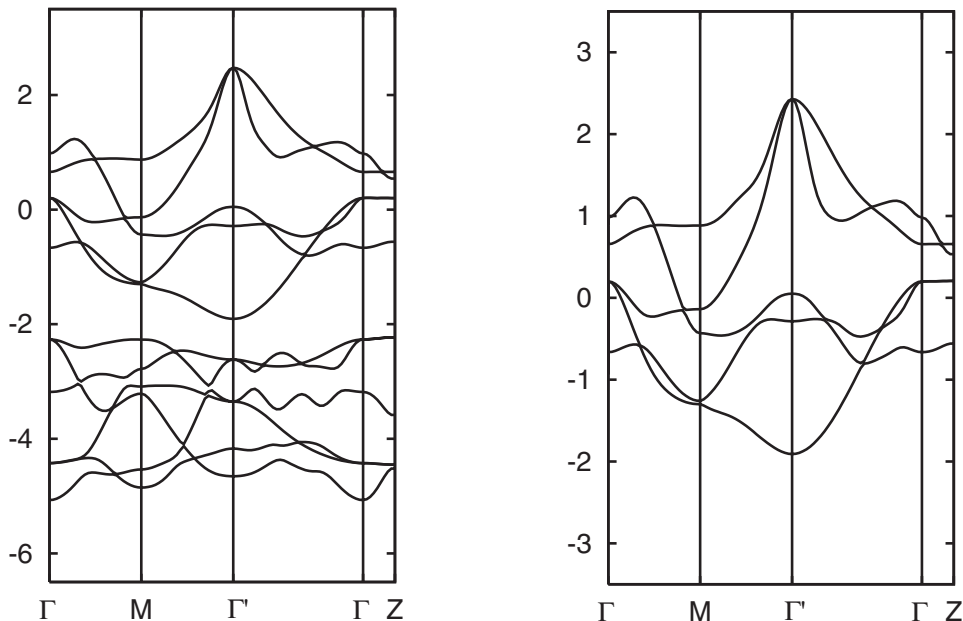


Fig. 8. Band dispersion of the *dpp* (left) and *d* model (right) for LaFeAsO with the first Brillouin zone being extended to the second Brillouin zone, so that the unit cell contains only one Fe atom. Both Γ and Γ' points correspond to Γ in the original band structure in Fig.6.

3.4. *FeSb₂*

FeSb_2 is a small band gap semiconductor which is intensively studied [38] for its unusually good thermoelectric properties. In order to describe the Coulomb interaction within the Fe-3d shell and the strong hybridization between the Fe-3d and the Sb-4p electrons on an equal footing, a Wannier projection onto a 22 band *pd* subspace is required. FeSb_2 has an orthorhombic structure belonging to the space group $58(Pnmm)$, in which the Fe sites are located at the centers of largely distorted Sb octahedra. This distortion results in a low point group symmetry at the Fe site.

The LDA bandstructure, shown (grey solid lines in Fig. 10), is rather complicated, with about 10 bands in the energy interval of $\pm 2\text{eV}$ around the Fermi level. The Wannier functions were constructed from 41 Bloch states on a $10 \times 10 \times 10$ \mathbf{k} -grid, by projection onto the subspace of 22 MLWF in the energy region $[-6\text{eV}, +6\text{eV}]$, using the disentanglement procedure of wannier90.

We performed Wannier projections with different frozen energy windows and found that already the window $[-6\text{eV}, 3.9\text{eV}]$ allows for a good description of all the 22 bands in the whole energy interval of $\pm 6\text{eV}$ around the Fermi level. The corresponding MLWFs are well localized with the spread ranging from 0.8\AA^2 to 1.2\AA^2 for Fe-3d orbitals and from 3.6\AA^2 to 5.0\AA^2 for the Sb-4p orbitals. The largest spread of $\simeq 1.2\text{\AA}^2$ was obtained for the two Fe- e_g -like Wannier functions which point more towards the direction of the ligands (see, e.g., first panel in the first row of Fig. 9), while the other three (Fe- t_{2g} -like) Wannier orbitals are slightly more localized with a spread of $0.8\text{\AA}^2 \div 1.0\text{\AA}^2$ (second and third panel of Fig. 9). The pictures of the three Sb-4p orbitals are reported with the same scale in the second row of Fig. 9. The contributions of the different MLWFs to the bandstructure is shown as a so-called fat-band plot in Fig. 10, revealing a strongly mixed *d-p* character of all bands.

By truncating the Hamiltonian in the MLWF basis set in direct space, we find that retaining hoppings up to 7.3\AA provides an accurate description of the LDA bands. A closer analysis shows that the strongest hopping processes ($1.2 \div 1.8$ eV) are in the *p-p* sector of the Hamiltonian. Relatively large hoppings are found also in the *p-d* sector (up to $0.6 \div 0.9$ eV) while the *d-d* hopping amplitudes reach the maximum value of about 300meV.

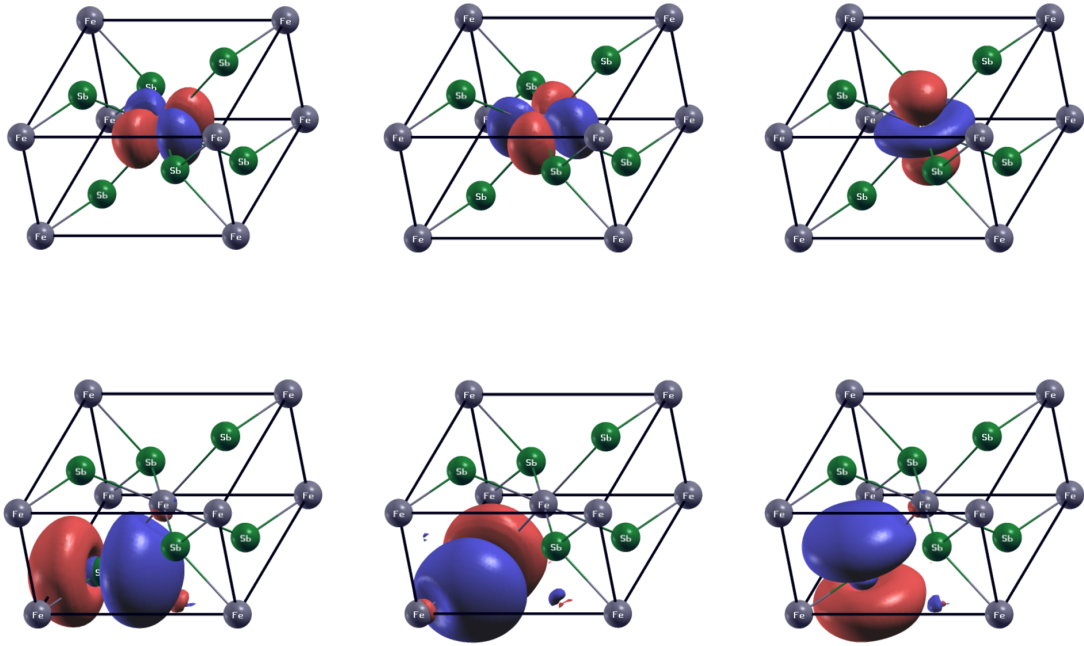


Fig. 9. (color online) The basis of Wannier orbitals in FeSb_2 , presented as an isosurface plot in real space within the coordinate system of the primitive unit cell. In the first row (from left to right), we show one of the orbitals with predominant e_g character (pointing approximately in the direction of the ligands) and two of the orbitals with mainly t_{2g} character, respectively. In the second row we show, from left to right, the p_x , p_y , p_z orbitals.

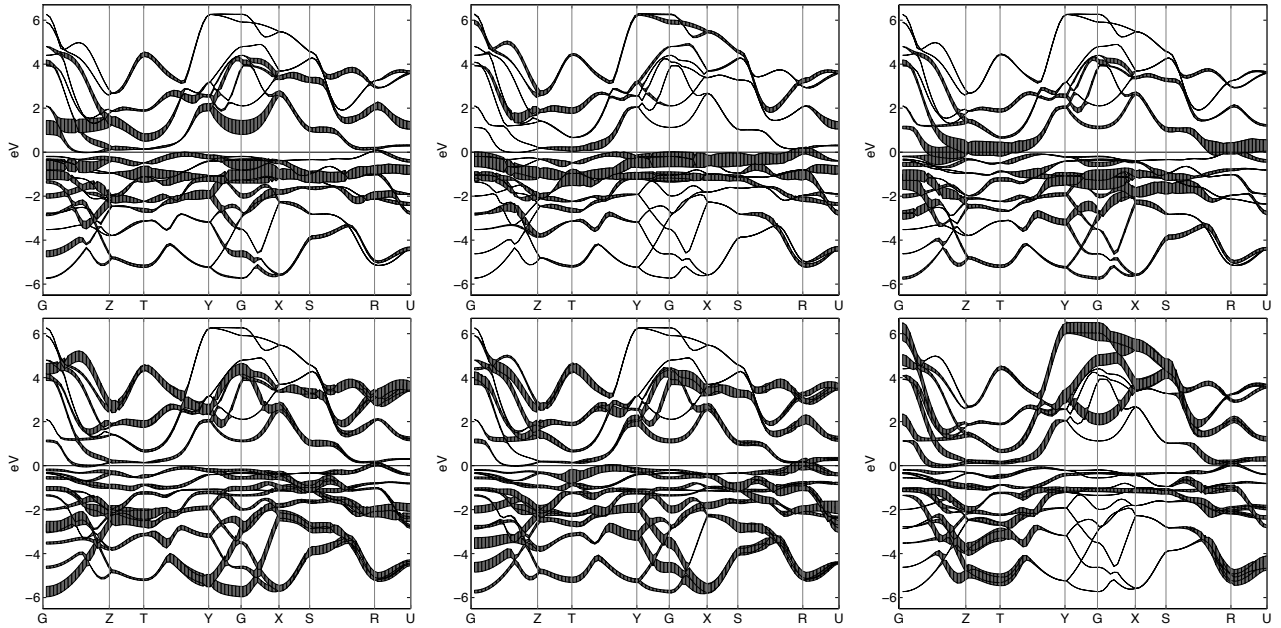


Fig. 10. Partial contributions to the bandstructure corresponding to the Wannier orbitals visualized in Figure 9. From top left to bottom right, the widths of the bands indicate the contribution of the e_g , $t_{2g}(e_g^\pi)$, $t_{2g}(a_{1g})$, p_x , p_y , and p_z Wannier function, respectively. Note the huge p - d hybridization in the energy region $[-4 \text{ eV}, 4 \text{ eV}]$.

4. Summary

We have presented the implementation of an interface between the FLAPW code Wien2K and wannier90 software for the construction of the maximally localized Wannier functions. The rationale of this development is to provide a link between two widely used packages in the electronic structure community. We tried to provide examples of what we consider typical applications of such a construction such as the construction of tight-binding Hamiltonians for complex systems, unfolding of complicated bandstructures or visualization. We also considered applications that have been so far less common such as strongly spin-orbit coupled Wannier orbitals. Last but not least we point out that the overlap matrices [Eq. (4)] can find application of its own, e.g. concerning the calculation of the interaction with an electro-magnetic field beyond the dipole approximation.

5. Acknowledgement

We would like to thank K. Schwarz, P. Blaha, P. Novák, K. Nakamura, and T. Miyake for discussions. J.K. acknowledges the support of the SFB 484 of the Deutsche Forschungsgemeinschaft and the grant no. P204/10/0284 of the Grant Agency of the Czech Republic. R.A. was supported by the Next Generation Supercomputing Project of Nanoscience Program from MEXT, Japan and the Funding Program for World-Leading Innovative R&D on Science and Technology (FIRST Program), K.H. by the EU-Indian cooperation network MONAMI, and P.W. through WK004 of the Austrian Science Foundation (FWF). J.K. and K.H. thank for hospitality of the Kavli Institute of Theoretical Physics and UC Santa Barbara.

References

- [1] G. H. Wannier, *Phys. Rev.* **52**, 191 (1937).
- [2] P. Hohenberg and W. Kohn, *Phys. Rev.* **136** B864 (1964); W. Kohn and L. J. Sham, *Phys. Rev.* **140** A1133 (1965); R. O. Jones and O. Gunnarsson, *Rev. Mod. Phys.* **61** 689 (1989); R. M. Martin, *Electronic Structure: Basic Theory and Practical Methods* (Cambridge University Press, 2004).
- [3] D. Vanderbilt and R. D. King-Smith, *Phys. Rev. B* **47**, 1651 (1993).
- [4] M. Marzari and D. Vanderbilt, in *First principle calculations for ferroelectrics: Fifth Williamsburg Workshop* (Springer Verlag 1998), p.146.
- [5] Y. Tokura, *Science* **312**, 1481 (2006).
- [6] T. Thonhauser, D. Ceresoli, D. Vanderbilt, and R. Resta, *Phys. Rev. Lett.* **95**, 137205 (2005).
- [7] M. Sharma, Y. Wu, and R. Car *International Journal of Quantum Chemistry* **95**, 821 (2003).
- [8] A. Calzolari, N. Marzari, I. Souza, M. B. Nardelli, *Phys. Rev. B* **69**, 035108 (2004).
- [9] K. S. Thygesen and K. W. Jacobsen, *Chemical Physics* **319**, 111 (2005).
- [10] E. Müller-Hartmann, *Z. Phys. B* **74** 507 (1989).
- [11] V. I. Anisimov, A. I. Poteryaev, M. A. Korotin, A. O. Anokhin and G. Kotliar, *J. Phys. Cond. Matter* **9**, 7359 (1997); A. I. Lichtenstein and M. I. Katsnelson, *Phys. Rev. B* **57**, 6884 (1998); G. Kotliar, S. Y. Savrasov, K. Haule, V. S. Oudovenko, O. Parcollet and C. A. Marianetti, *Rev. Mod. Phys.* **78**, 865 (2006); K. Held, *Adv. Phys.* **56**, 829 (2007).
- [12] O. K. Andersen, *Phys. Rev. B* **12** 3060 (1975).
- [13] O. K. Andersen, T. Saha-Dasgupta, R. W. Tank, C. Arcangeli, O. Jepsen and G. Krier, In *Lecture notes in Physics*, edited by H. Dreyse (Springer, Berlin, 1999); O. K. Andersen, T. Saha-Dasgupta, S. Ezhov, L. Tsetseris, O. Jepsen, R. W. Tank and C. A. G. Krier, *Psi-k Newsletter* **# 45** 86 (2001).
- [14] N. Marzari and D. Vanderbilt, *Phys. Rev. B* **56**, 12847 (1997).
- [15] I. Souza, N. Marzari and D. Vanderbilt, *Phys. Rev. B* **65**, 35109 (2001).
- [16] A. A. Mostofi, J. R. Yates, Y.-S. Lee, I. Souza, D. Vanderbilt and N. Marzari *Comput. Phys. Commun.* **178**, 685 (2008); www.wannier.org.
- [17] F. Lechermann, A. Georges, A. Poteryaev, S. Biermann, M. Posternak, A. Yamasaki, O.K. Andersen, *Phys. Rev. B* **74**, 125120 (2006).
- [18] T. Miyake and F. Aryasetiawan, *Phys. Rev. B* **77**, 085122 (2008).
- [19] M. Posternak, A. Baldereschi, S. Massidda, and N. Marzari, *Phys. Rev. B* **65**, 18442 (2002).
- [20] F. Freimuth, Y. Mokrousov, D. Wortmann, S. Heinze, and S. Blügel *Phys. Rev. B* **78**, 035120 (2008).
- [21] W. Ku, H. Rosner, W. E. Pickett, and R. T. Scalettar, *Phys. Rev. Lett.* **89**, 167204 (2002).
- [22] V.I. Anisimov, D.E. Kondakov, A.V. Kozhevnikov, I.A. Nekrasov, Z.V. Pchelkina, J. W. Allen, S.-K. Mo, H.-D. Kim, P. Metcalf, S. Suga, A. Sekiyama, G. Keller, I. Leonov, X. Ren, D. Vollhardt, *Phys. Rev. B* **71**, 125119 (2005).

- [23] M. Aichhorn, L. Pourovskii, V. Vildosola, M. Ferrero, O. Parcollet, T. Miyake, A. Georges, and S. Biermann Phys. Rev. B **80**, 085101 (2009).
- [24] P. Blaha, K. Schwarz, G.K.H. Madsen, D. Kvasnicka, J. Luitz, WIEN2K, An Augmented Plane Wave and Local Orbitals Program for Calculating Crystal Properties, Vienna University of Technology, Austria, 2001; P. Blaha, K. Schwarz, P. Sorantin, S.B. Trickey, Comput. Phys. Commun. 59 (1990) 399.
- [25] http://www.wien2k.at/reg_user/unsupported/wien2wannier
- [26] <http://www.xcrysden.org/>
- [27] D.J. Singh, Planewaves, Pseudopotentials and the LAPW Method, Kluwer Academic, Boston, 1994.
- [28] E. Sjöstedt, L. Nordström, D.J. Singh, Solid State Commun. 114 (2000) 15; G.K.H. Madsen, P. Blaha, K. Schwarz, E. Sjöstedt, L. Nordström, Phys. Rev. B 64 (2001) 195134.
- [29] Y. Kamihara, T. Watanabe, M. Hirano, H. Hosono, J. Am. Chem. Soc. 130 (2008) 3296.
- [30] K. Kuroki, S. Onari, R. Arita, H. Usui, Y. Tanaka, H. Kontani, H. Aoki, Phys. Rev. Lett. 101 (2008) 087004.
- [31] C. Cao, P.J. Hirschfeld, C. Hai-Ping, Phys. Rev. B. 77 (2008) 220506.
- [32] K. Nakamura, R. Arita, M. Imada, J. Phys. Soc. Jpn. 77 (2008) 093711.
- [33] V. Vildosola, L. Pourovskii, R. Arita, S. Biermann, A. Georges, Phys. Rev. B 78 (2008) 064518.
- [34] V. I. Anisimov, Dm. M. Korotin, M. A. Korotin, A. V. Kozhevnikov, J. Kuneš, A. O. Shorikov, S. L. Skornyakov, S. V. Streltsov, J. Phys.:Condens. Matter 21 (2009) 075602.
- [35] M. Miyake, K. Nakamura, R. Arita, M. Imada, to appear in J. Phys. Soc. Jpn.
- [36] R. Arita, H. Ikeda, J. Phys. Soc. Jpn 78 (2009) 113707.
- [37] H. Ikeda, R. Arita, J. Kuneš, Phys. Rev. B. 81 (2010) 054502.
- [38] A. Bentien, G. K. H. Madsen, S. Johnsen, B. B. Iversen, Phys. Rev. B 74(2006) 205105; A. Bentien, S. Johnsen, G. K. H. Madsen, B. B. Iversen, F. Steglich, Eur. Phys. Let. 80(2007) 17008; C. Petrovic, Y. Lee, T. Vogt, N. Dj. Lazarov, S. L. Budko, P. C. Caneld, Phys. Rev. B 72(2005) 045103.